



Investigation of Cracking Susceptibility and Porosity Formation and Its Mitigation Techniques in Laser Powder Bed Fusion of Al 7075 Alloy

Mayank Patel¹ · Akash Aggarwal¹ · Arvind Kumar¹

Received: 25 October 2022 / Accepted: 3 January 2023 / Published online: 6 February 2023
© The Author(s) under exclusive licence to The Korean Institute of Metals and Materials 2023

Abstract

The processing of high-strength Al7075 alloy through the laser powder bed fusion process is challenging because of cracking susceptibility. In this work, an experimental study has been carried out to understand the defects formation and to predict the optimum conditions for defect-free parts by varying process parameters such as laser power, scanning speed, base-plate heating temperature, remelting speed, and powder composition. A detailed mechanical and microstructural characterization has been carried out to investigate porosities, cracks, microstructure, grain structure, and mechanical properties. It was observed that the single-melting-based fabrication of Al7075 samples results in excessive porosities and solidification cracks along the build direction. The cracks are due to the insufficient liquid back-filling of the long columnar-dendritic grains during the solidification. The ramped-down high-speed remelting eliminates the balling defect, decreases the porosity percentage, and reduces surface roughness. The base plate heating of 473 K and 573 K reduces the extent of porosity and crack formation. Adding 4 wt% nano-TiC reinforcement to the Al7075 matrix eliminates the porosity and solidification cracks due to the very fine equiaxed grain because of heterogeneous nucleation.

Keywords Laser powder bed fusion · Al7075 alloy · Solidification cracking · Ramped down high-speed remelting · Nano-reinforcement

1 Introduction

Laser Powder Bed Fusion (LPBF) is a layer-by-layer additive manufacturing (AM) process that involves the selective melting of powder bed using a high-energy laser beam based on the slices generated from the 3D CAD model. LPBF is a preferred technique for processing various alloys because of its ability to achieve superior quality and dimensional accuracy compared to the other AM techniques available [1, 2]. Laser-matter interaction, melt kinetics and instability, laser scattering and attenuation, denudation, multiple laser reflections (powder bed and keyhole), recoil pressure-induced keyhole depression, melt pool flow, thermal history, surface impurity driven flows, spatters and powder particles induced beam shadowing, porosity generation, a transition of phases, wetting dynamics, surface tension, and the roughness

induced by spatters are the various phenomenon which affects the LPBF process [3, 4]. Due to these complex physical phenomena, processing Aluminium alloys (except AlSi10Mg and Al-12Si) is difficult by LPBF, and fabricated part suffers from problems such as solidification cracking, balling-induced porosities, and poor surface finish [5]. Al7075 is a high-strength, lightweight aluminum alloy rarely fabricated with LPBF because of severe solidification cracking. The cracks formed in Al7075 because of the high coefficient of thermal expansion and wide solidification range, which led to the micro-segregation tendency to occur during solidification [6, 7]. Louvis et al. [8] reported the rapid creation of the thin oxide layer on the liquid and solid surfaces and found that shattering the films using a high laser power and scan speed is necessary to prevent the effects of this film and the high conductivity of the crack-prone Al alloys. As a result, special care must be taken while setting process parameters to account for the Al alloy's high sensitivity towards hot cracking (i.e., liquation cracking and solidification cracking). Eskin et al. [9] predicted 6–8 vol% solidification shrinkage for the aluminum alloys, which is far higher than the 3 vol% shrinkage for the steel and titanium alloys

✉ Arvind Kumar
arvindkr@iitk.ac.in

¹ Additive Manufacturing Group, Department of Mechanical Engineering, Indian Institute of Technology Kanpur, Kanpur 208016, India

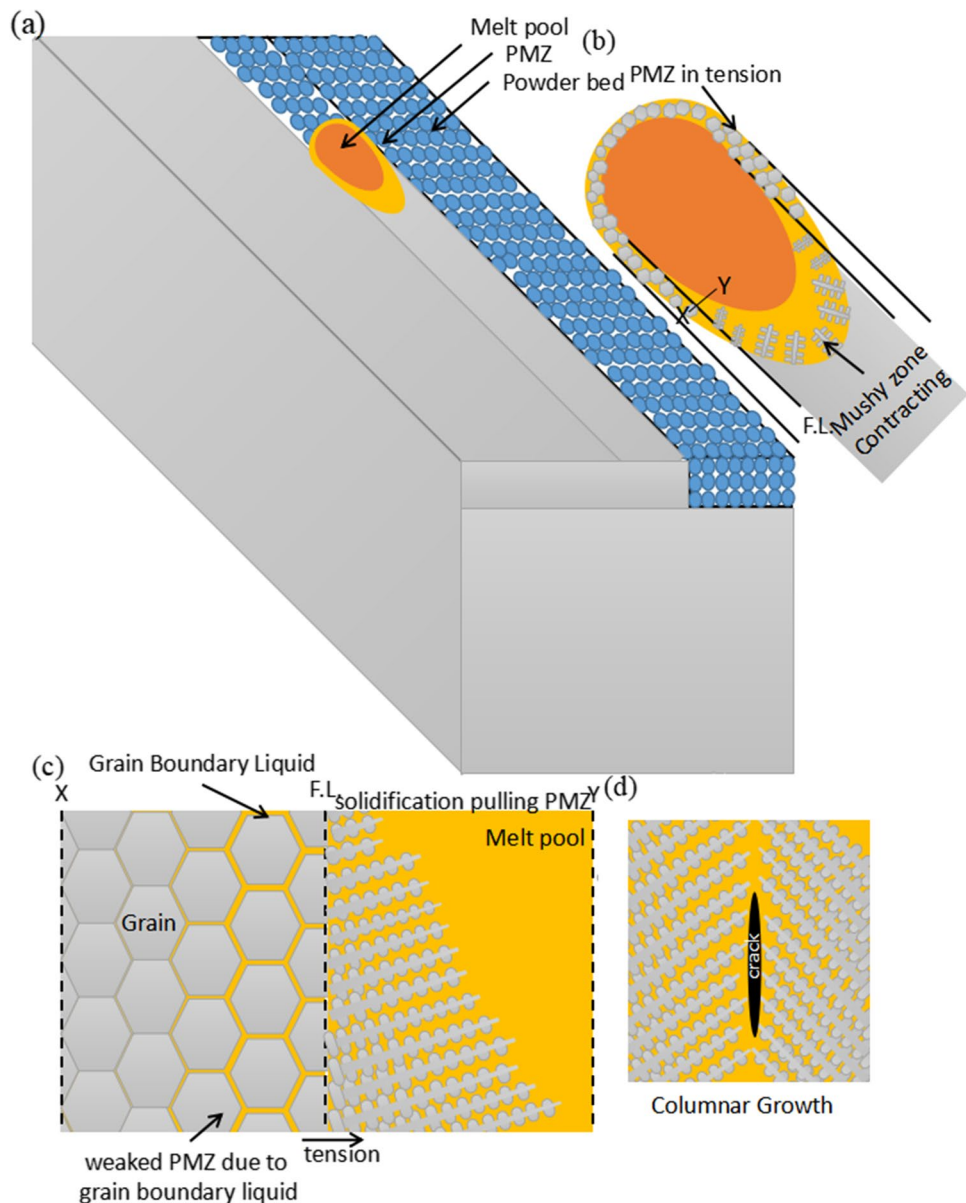
reported by Moiseyev et al. [10]. The Al7075 cracking susceptibility can be evaluated by the index $\left|dT/df_s^{1/2}\right|$ at $f_s^{1/2} = 1$, where T is the mushy zone temperature and f_s is the solid fraction. This index is known as Kou's criterion [11]. This index for Al7075 is higher than Al2024 and Al2219 alloys and lower than Al6061 alloys [12]. Excessive or insufficient energy input under too low or too high scan speed led to an unstable molten pool, which produced the spatter phenomena during LPBF, according to Guo et al. [13]. The rapid solidification of the molten powder layer generates cellular dendritic and columnar grains with epitaxial growth [14].

The LPBF schematic and melt pool region are shown in Fig. 1a, b respectively. There are mainly two types of

cracking observed in the LPBF process i.e. solidification cracking and liquation cracking. The solidification cracking occurs because of the lack of liquid back-filling between the long columnar grain boundaries channel, as shown in Fig. 1d. These channels are created because of the high forward growth of the cell-dendritic compared to the low lateral growth of bridging the cells. The interdendritic micro-segregation of the alloying elements also increases the cracking susceptibility because of the constitutional undercooling condition [15–17].

Liquation cracking was caused by constitutional liquation, which is defined as a non-equilibrium melting of intermetallic phase particles at grain boundaries at temperatures between the eutectic and solidus temperature [18], as illustrated in Fig. 1c. The lack of dissolving of intermetallic

Fig. 1 Schematic representing the **a** LPBF process, **b** zoomed view of melt pool region, mechanism of different cracking **c** liquation cracking in the mushy zone [21], **d** solidification cracking



phase particles is because of a multi-phase alloy heated very fast to solution temperature, resulting in a short period to achieve eutectic temperature [19]. The crack is initiated under the tensile stresses at a liquid film of grain boundaries generated by the constitutional liquation. Thus, in Al7075 SLM, a liquation crack interferes with a solidification crack. Ghaini et al. [20] reported work of Al2024 alloys, which suggests that the liquation crack can strongly affect the solidification crack initiation.

Reschetnik et al. [22] optimized the process parameters for fabricating the Al7075 specimens. However, the fabricated specimens still contain long cracks, mostly initiated in a fusion zone and produced along the direction of the building. Stopyra et al. [23] investigated the influence of the process parameter on hot cracking and porosity without changing the Al7075 composition. A density of around 99% was achieved by applying the Hot Isostatic Pressing (HIP) to the specimens fabricated at optimum process parameters. It was observed that the HIP reduced the small cracks but did not influence the long cracks along the build direction. Kaufmann et al. [24] utilized the base plate preheating technique to prevent the solidification crack during the LPBF process. The base plate heating reduces the thermal gradients and decreases the undercooling and thermal stresses. The authors achieved 99.8% density for Al7075 alloy by using a high-power laser and 200 °C base plate heating; however, the complete elimination of the cracks was not achieved. Similarly, Mertens et al. [25] achieved crack reduction and change in crack morphology by preheating at 400 °C, still, complete elimination of cracks was not achieved.

Remelting is a useful technique for enhancing the surface quality and managing imperfections. The solidified layer is remelted to achieve defect-free and high surface quality of LPBF fabricated parts. According to Brodie et al. [26], LPBF of Ti25Ta fabricated samples yield strength increased from 426 ± 15 to 545 ± 9 MPa after remelting, and the material homogeneity was enhanced. Zhang et al. [27] employed remelting on four common LPBF alloys, including 316L SS, AlSi10Mg, IN 718, and Ti6Al4V, and found that the surface roughness was reduced. Remelting was used by Ghorbani et al. [28] to enhance the quality of inclined surfaces on 316L inclined components produced by LPBF. A two-dimension model was created by Shen et al. [29] to investigate how remelting treatment affected the disappearance of pore defects. The relationship between the development of the pore defect and the laser energy density was also addressed in detail. Yu et al. [30] fabricated remelted 17-4 PH stainless steel that had been laser direct metal deposited, they discovered that the pre-solidified microstructure had been significantly diluted. Surface porosity and roughness both might be greatly reduced. For direct energy deposited Inconel 625, Koike et al. [31] used the remelting procedure to regulate the metal crystal orientation and lingering

pore defect. Zhou et al. [32] investigated laser remelting to enhance the surface quality for AlSi10Mg using LPBF.

The controlled nucleation and crystal grain growth prevent the crack formation in the 6xxx and 7xxx alloys during the LPBF process because of the generation of small equiaxed grains [33]. According to Hunt's criterion of columnar to equiaxed grain transition, significant undercooling is required for the generation of nucleation and equiaxed grains, which is generated by manipulating thermal gradients and local solidification velocity [34]. Undercooling in the LPBF of Aluminum alloys is especially challenging due to the alloying element's rapid solidification rate, high thermal conductivity, and effective liquid diffusivity. Melt movement [35] and acoustic cavitation method [36] have the potential to generate equiaxed grains by fragmenting columnar dendritic grains. The work reported by Martin et al. [37] shows no cracks in the LPBF of Al7075 alloys because of the addition of reinforcement to promote the heterogeneous nucleation that results in a reduction of the undercooling threshold for the growth of the equiaxed grains. They developed nano-functionalized hydrogen-stabilized zirconium nanoparticle-based powders, which produced the Al₃Zr nucleate phase after the decomposition of the melt. However, because aluminum alloys are vulnerable to hydrogen embrittlement, the usage of hydrogen may be problematic. Porosity can also be caused by the variation in hydrogen solubility in solids and liquids. Other researchers have also utilized the reinforcement addition technique. Bi et al. [38] created a novel Sc and Zr-modified 7075 Al alloy with grain refinement for crack defect elimination. Montero-Sistiaga et al. [39] customized Al7075 alloy by manually mixing 4 wt% Si into LPBF-produced Si/Al7075 composites to prevent cracks. Wu et al. [40] investigated the microstructure, mechanical characteristics, and crack elimination process of LPBF-fabricated TiN/Al7075 composites. Tan et al. [41] achieved a crack-free, fine-equiaxed microstructure in the LPBF-fabricated 7075 alloy using a combination of substrate alteration and Ti inoculation possesses mechanical qualities equal to its wrought counterpart.

It can be concluded from the aforementioned points that the fabrication of defect-free Al7075 parts is challenging. Optimizing process parameters for manufacturing defect-free parts of Al7075 alloys is a complex task because of the lack of understanding of the cracking and porosity formation behavior in LPBF processing of Al7075. Consequently, there is a scarcity of data on optimum processing strategies that can produce defect-free parts of this alloy.

This work uses an experimental study to fabricate Al7075 alloy using a low laser energy density based commercial LPBF setup. Firstly, Al7075 bulk samples were fabricated using a combination of ramped-down high-speed remelting, high-temperature base plate heating, and the TiC nano-reinforcement addition. Then, a detailed mechanical and

microstructural characterization was carried out using optical microscopy, X-ray diffraction (XRD), high-resolution X-ray microtomography, Energy Dispersive Spectroscopy (EDS), optical profilometry, Scanning Electron Microscopy (SEM), mechanical testing to investigate porosities, elongated submicron-wide solidification cracks, microstructure, grain structure, and mechanical properties.

2 Materials and Methods

2.1 Materials

Gas-atomized Al7075 powder (Carpenter Additive, U.K.) with a nearly spherical morphology (Fig. 2a–c) was used to fabricate the bulk specimens by the LPBF process. The powder size distribution was studied by the laser diffraction particle size analyzer (Mastersizer 2000, Malvern Instruments). The measured powder size distribution is shown in Fig. 3. The measured Al7075 powder values of D_{10} , D_{50} , and D_{90} are 26.56 μm , 41.37 μm , and 64.60 μm , respectively. Table 1 represents the chemical composition of the Al7075 powder.

2.2 Preparation of Al7075-TiC Metal Matrix Composite

For the preparation of Al7075 metal matrix composites bulk specimens, 4 wt% nano-TiC powder (99.9% purity, $D_{50} = 80 \text{ nm}$, density = 4.93 g/cm^3) was mechanically mixed for 4 h at a speed of 200 RPM [42] with the Al7075 matrix ($D_{10} = 26.56 \text{ }\mu\text{m}$, $D_{50} = 41.37 \text{ }\mu\text{m}$, $D_{90} = 64.60 \text{ }\mu\text{m}$). To avoid plastic deformation and maintain the roundness of aluminum powders, balls were not used in the mechanical mixing process. After the mechanical mixing process, the nano TiC particles are evenly spread over the Al7075 alloy powders as shown in Fig. 2e, f. Figure 2g–i shows the reinforced powder particle's Energy Dispersive Spectroscopy (EDS) map and the element distribution maps (Fig. 2h—Al and Fig. 2i—Ti).

2.3 Samples Fabrication

Al7075 bulk samples were fabricated using the commercial LPBF machine (GE Additive Concept Laser Mlab R) equipped with a continuous-wave Yb fiber 100 W laser with a focused beam diameter of 50 μm . Firstly, a preliminary study (without remelting, without base plate heating, and without adding nano-reinforcement) was conducted to find the optimum process parameters which result in the maximum possible density for Al7075 samples. The optimum process parameters which result in the maximum density (88.24%) are listed in Table 2. Further, improvement in the density is not possible with the current commercial LPBF setup due to the constraints of the maximum laser power and

the minimum laser scanning speed. Therefore, to improve the density and decrease the defects (porosity and cracks), solidification conditions (temperature gradient, solidification rate, and nucleation density) were modified by applying a combination of ramped-down high-speed remelting, high-temperature base plate heating, and the nano-reinforcement mixing (4 wt% TiC reinforcement addition).

A temperature control base plate heating setup was designed as shown in Fig. 4. The heating setup was integrated with the commercial LPBF machine (Concept Laser Mlab R). The heating setup consists of a base plate heating module, a voltage regulator, and a Proportional Integral Derivative (PID) controller. The base plate heating module consists of a copper block in which two cartridge heaters were fitted. The aluminum build plate is held over the top surface of the copper block. Thermo-couples are fitted to the aluminum base plate to monitor and control a constant heating temperature via a PID controller. A total of 12 cuboidal samples with varying process parameters (Tables 2 and 3) were fabricated to investigate the influence of remelting, base plate heating, and nano-reinforcement on the defects and the microstructure. The constant process parameters used for the fabrication of the samples are listed in Table 2, and the varying process parameters are listed in Table 3.

2.4 Characterization

The fabricated bulk specimens were cross-sectioned along the build direction with a wire-electric discharge machine for defects and microstructural analysis. Then standard metallographic grinding and polishing were carried out. The optical microscopy of the polished samples was carried out to quantify the defects (porosity and cracks) and to measure the relative density of the parts. After that, the polished samples were etched using Keller's etchant to visualize the microstructure and the melt pool boundaries. Field-Emission Scanning Electron Microscopy (Mira3 FESEM, TESCAN) with the Energy Dispersive Spectroscopy (EDX) setup was used to visualize the microstructure and the elemental composition. The phases in the powder particles and the fabricated bulk samples were characterized using an X-ray diffractometer (MiniFlex 600, Rigaku). The 2θ angle for the X-ray diffraction varied from 30° to 100° with a time step of 0.02° . X-ray micro-tomography (Xradia Versa 520, Zeiss) of the fabricated bulk specimens was carried out to examine the 3D distribution of cracks and porosity. The X-ray source power, voltage, step rotation angle, and voxel size were 8 W, 150 kV, 0.45° , and 2.12 μm , respectively. The reconstructed images were segmented with the help of the Weka 3D segmentation tool in open-source ImageJ software. ImageJ and open-source 3D slicer software were utilized for pore measurement and 3D volume rendering. Room temperature Vickers hardness measurements of the fabricated bulk

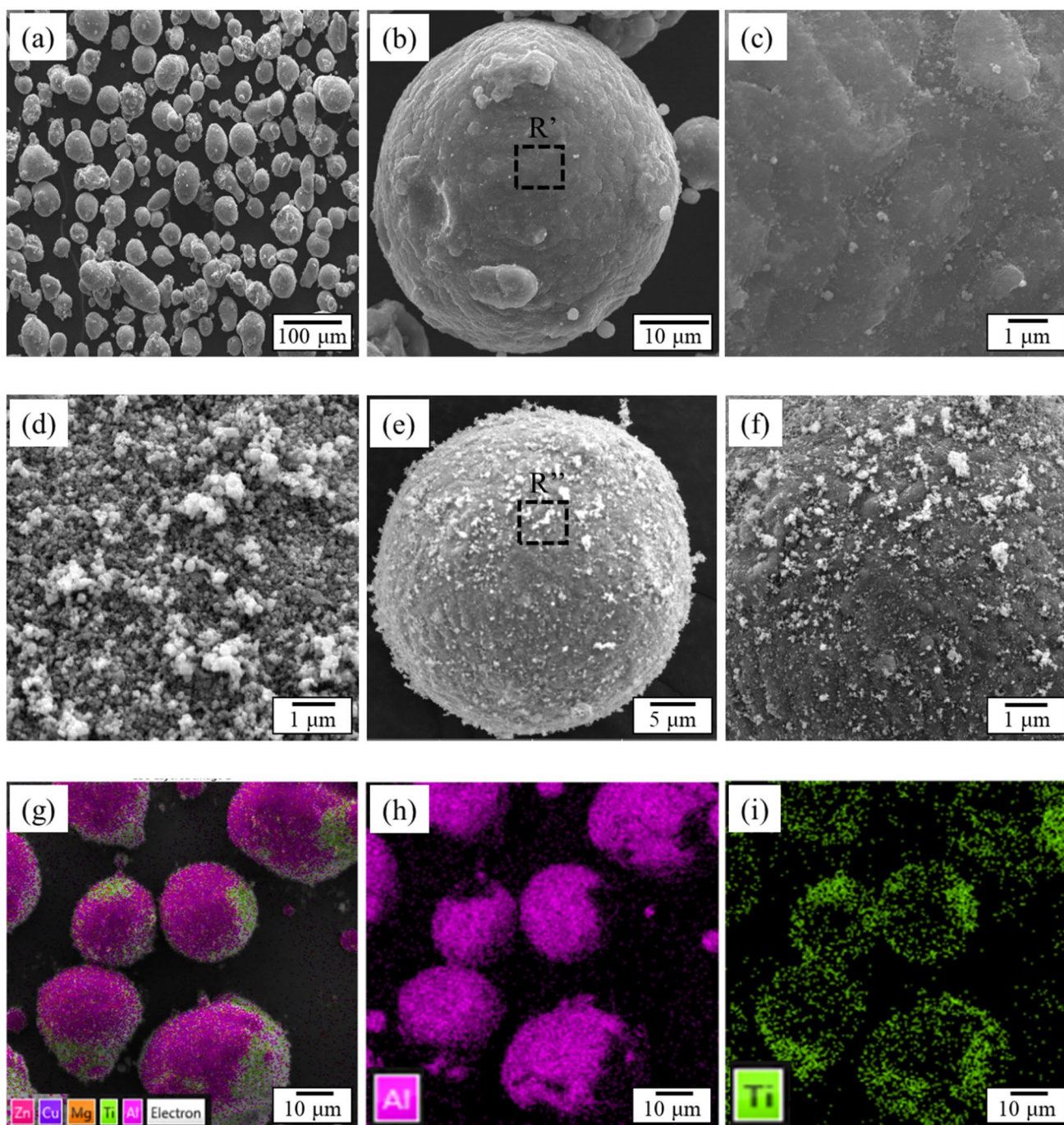


Fig. 2 Scanning electron micrographs of powder particles **a** Al7075 powder, **b** magnified image of single Al7075 powder particle, **c** magnified image of region R' in **b**, **d** TiC powder, **e** magnified image of a reinforced Al7075 powder particle (Al7075+4 wt% TiC), **f** magni-

fied image of region R'' in **e**. Energy dispersive spectroscopy (EDS) color maps: **g** Al7075+4 wt% TiC, **h** elemental map of Al, and **i** elemental map of Ti

specimens were performed using a micro-hardness tester (Micro-indentation Tester, CSM International) at a load of 50 gf and a dwell time of 10 s. For each specimen, five readings were taken. Room temperature tensile tests were conducted on a universal testing machine (Instron-1195) with a 1 mm/min crosshead speed. The surface morphology of the

top surface of the bulk specimen was quantified with the 3D optical profilometer (Nano Map-D). The surface roughness analysis was carried out using the MountainsLab® software. The electron backscatter diffraction (EBSD) scans were performed at a 20 kV accelerating voltage and a 0.75 μm step size.

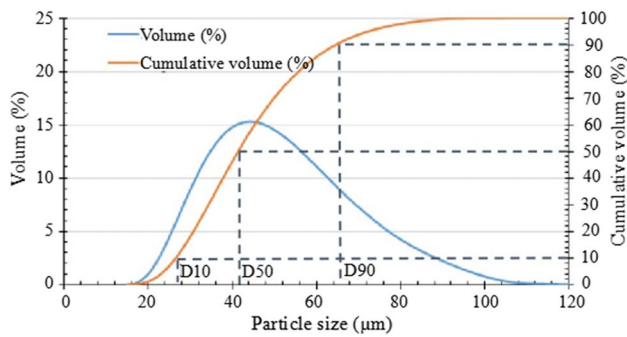


Fig. 3 Powder size distribution of Al7075 powder obtained by laser diffraction particle size analyzer

3 Results and Discussions

3.1 Melt Pool Shape and Defects Behavior: Optical Microscopy Results

Figure 5 shows the optical micrographs in the upper region of the etched Al7075 samples (*S1*, *S2*, *S3*, *S7*, *S8*, and *S9*). The single melting sample (*S1*) shows a rough and wavy surface topography, which can hinder the uniform spreading of the subsequent powder layers and eventually lead to the formation of large irregular-shaped porosities. The rough surface topography for a single melting sample is because of the balling defects due to insufficient applied laser energy density. The surface waviness is substantially reduced for the ramped-down remelting cases (*S2* and *S3*, Fig. 5b, c). The ramped-down high-speed remelting melts and smoothen the balling defects, which arise after the 1st melting. This results in a smooth spreading of the subsequent powder layers. The single melting case (*S7*, Fig. 5d) with base plate heating of 573 K also has wavy surface topography, but the extent is less than the room temperature single melting sample (*S1*, Fig. 5a). This is because base plate heating provides additional input energy to melt the powder, resulting in a low-balling defect. The ramped remelting with base plate heating (*S8* and *S9*, Fig. 5e, f) also reduces the surface roughness. The melt pool boundaries for the single melting and the high-speed ramped-down remelting can be observed

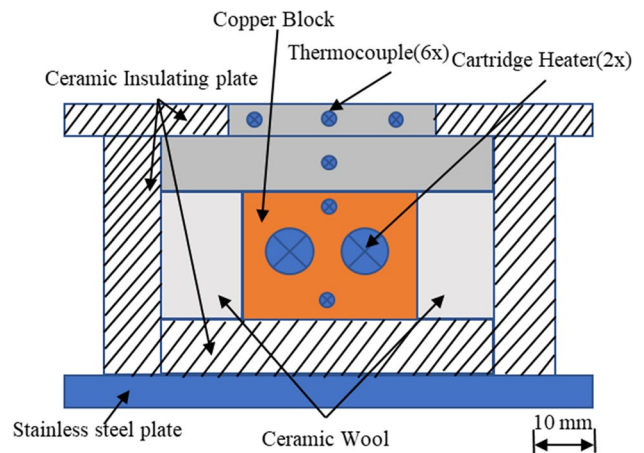


Fig. 4 Schematic of the high-temperature base plate heating setup

in Fig. 5. The base plate heating results in a bigger melt pool (Fig. 5d–f) than the sample fabricated without the base plate heating (Fig. 5a–c).

Figure 6 shows the optical micro-graphs along the build direction for all the process parameters and fabrication conditions (single melting, ramped-down high-speed remelting, high-temperature base plate heating, and TiC nano-reinforcement addition in feedstock Al7075 powder). The sample density for each case is mentioned in the box at the bottom-right corner.

We used a commercial LPBF (GE Concept Laser Mlab R) machine with a maximum laser power of 100 W. In the current study, cubical samples with dimensions of 10 mm × 10 mm × 10 mm were fabricated with scan speeds ranging from 100 mm/s to 500 mm/s, while the other parameters remained constant (i.e., laser power, $P=95$ W, hatch spacing = 56 µm, layer thickness = 40 µm, scanning pattern = Island). Because Al7075 has a high reflectivity (45.2% at wavelength 1064 nm) [40] and thermal conductivity (130 W/m·K) [23], the selected laser power of 95 W is insufficient to melt the powder layer properly even at low scan speed. We chose 200 mm/s as the least damaged parameter because any further reduction in scanning speed cause extensive balling and spattering issues. As a result, with the current commercial 100 W LPBF setup, improvement in

Table 1 The chemical composition of the Al7075 alloy powder

Element	Cu	Cr	Mg	Zn	Fe	Mn	Si	Ti	Others	Al
wt%	1.6	0.2	2.4	5.4	0.13	0.1	0.1	0.1	0.1	89.96

Table 2 Optimized single melting process parameters for the LPBF fabricated cuboidal samples of Al7075 alloy

Process parameters	Laser power	Laser beam diameter	Scanning speed (1 st melting)	Layer thickness	Hatch spacing	Scanning strategy
Values	95 W	50 µm	200 mm/s	40 µm	56 µm	Island

Table 3 Process parameters for the LPBF fabricated cuboidal samples (Sample 1 to sample 12)

Sample ID	Scanning speed (First melting) (mm/s)	Scanning speed (Re-melting) (mm/s)	Base plate heating temperature (°C)	TiC nano-reinforcement (wt%)
<i>S1</i>	200	–	–	–
<i>S2</i>	200	800	–	–
<i>S3</i>	200s	1600	–	–
<i>S4</i>	200	–	200	–
<i>S5</i>	200	800	200	–
<i>S6</i>	200	1600	200	–
<i>S7</i>	200	–	300	–
<i>S8</i>	200	800	300	–
<i>S9</i>	200	1600s	300	–
<i>S10</i>	200	–	–	4
<i>S11</i>	200	800	–	4
<i>S12</i>	200	1600	–	4

density for the single melting case is not possible. Therefore, to improve the density and reduce defects (porosity and cracks), the solidification conditions (temperature gradient, solidification rate, and nucleation density) were modified using ramped-down high-speed remelting, high-temperature base plate heating, and by adding TiC nano-reinforcement. The high-speed ramped-down remelting (*S2*, Fig. 6b, and *S3*, Fig. 6c) eliminates the porosity due to the lack of fusion, and only micro-porosity remains. However, the number of micron-scale wide solidification cracks increases. High-temperature base plate heating of 473 K and 573 K results in a slight increase of density to 89.60% and 93.56%, respectively, for single melting cases (*S4*, Fig. 6d, and *S7*, Fig. 6g). The cases (*S9*, Fig. 6i) in which high-temperature base plate heating is applied along with the high-speed ramped down remelting result in a substantial reduction in the porosity and density increase to 96.09%. The number of cracks decreases but the size of the cracks increases. Figure 6j–l shows that adding 4 wt% TiC nano-reinforcement to the Al7075 matrix eliminates the cracking for cases *S10*, *S11*, and *S12*. The single melting case (*S10*, Fig. 6j) still has some large irregular-shaped porosity. These large porosities completely disappear with the ramped-down remelting (*S11*, Fig. 6k, and *S12*, Fig. 6l). The maximum density of 99.71% without any solidification cracks is achieved for *S12* ($P=95$ W, $v_{1st}=200$ mm/s, $v_{2nd}=1600$ mm/s).

3.2 3D Defect Behavior: X-ray Tomography Results

Figure 7 shows the reconstructed 3D volume-rendered micro-tomography results for samples *S1* and *S12*. The imaging is done for LPBF-fabricated cylindrical samples of 2 mm in height and 2 mm in diameter. The fabricated sample with single melting at room temperature

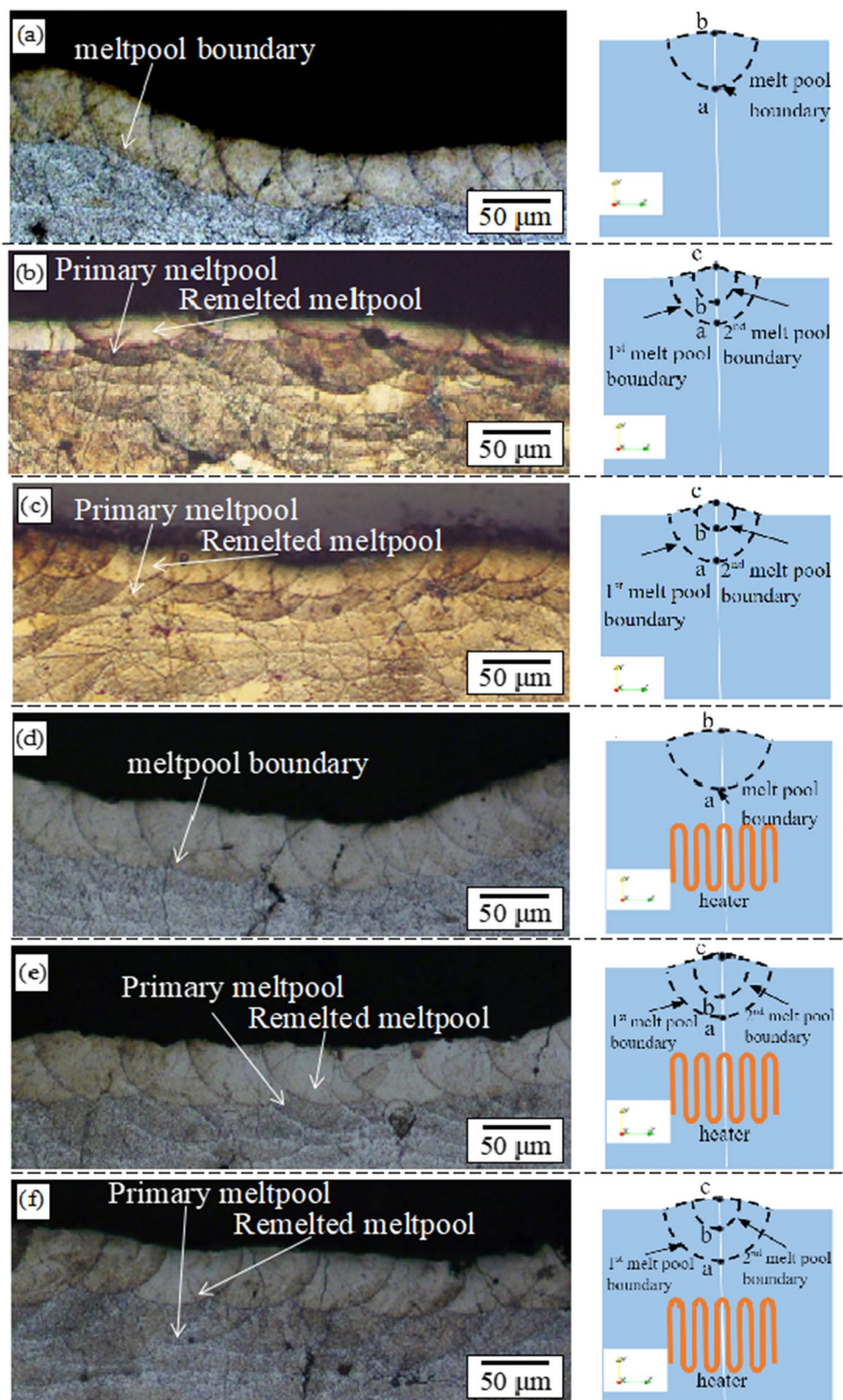
(*S1*, Fig. 7a) shows large quantities of defects (cracks and irregularly shaped porosities). In contrast, as shown in *S12*, Fig. 7b, there is a substantial reduction in the defects (cracks and porosity) when the ramped remelting technique with the nano-reinforcement addition is used to fabricate the Al7075 samples.

3.3 Surface Topography and Surface Roughness Analysis

The irregularities over the fabricated sample surfaces were assessed using 3D surface topography measurements with the help of a 3D optical profilometer. Figures 8a–c show the topography images for *S1*, *S2*, and *S3*. The surface roughness parameters S_a (arithmetic mean value) and S_q (root mean square value) are also mentioned in the figure. The surfaces were made up of a sequence of peaks and pits that corresponded to the laser direction. In each sample, the magnitude of the abnormalities varied. This was due to the material's flow inside a melt pool, solidification during sample fabrication, and the layer placement orientation, indicating the anisotropy of LPBF fabricated samples. It is essential to note that remelting produces smooth surface characteristics. The abnormalitie's height decreased with remelting, as seen by the decline for *S1* to *S3* in S_q from 23 to 16.5 μm and S_a from 17.5 to 12.4 μm .

The linear roughness values were also measured using a contact-type mechanical profilometer. The results are listed in Table 4. As observed from surface profilometry, remelted LPBF samples have a better finish than the single melted *S1* LPBF sample. The *S2* sample has a 30.5% higher surface quality, whereas the *S3* sample has a 52.88% higher surface quality than the *S1*.

Fig. 5 Optical micrograph of a vertical cross-section along the build direction with a graphical representation of cases **a** S1, **b** S2, **c** S3, **d** S7, **e** S8, and **f** S9



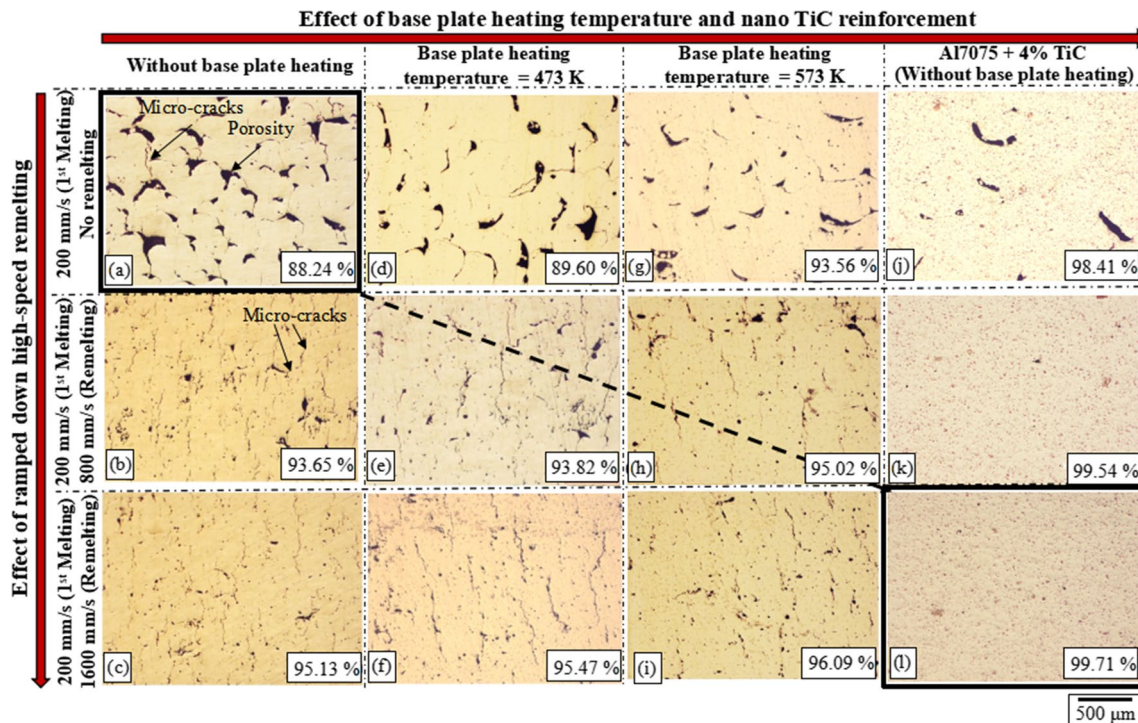
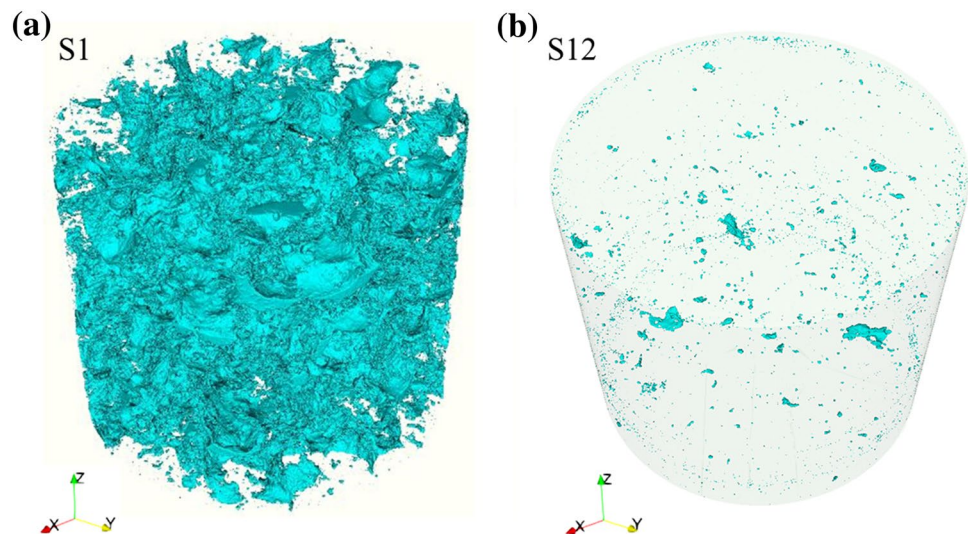


Fig. 6 Optical micrograph of a vertical cross-section of fabricated samples with process parameters shown in Table 3 **a** S1, **b** S2, **c** S3, **d** S4, **e** S5, **f** S6, **g** S7, **h** S8, **i** S9, **j** S10, **k** S11, **l** S12

Fig. 7 3D Volume rendered tomography images showing defects for samples **a** S1 and **b** S12. (Sample dimension: Diameter: 2 mm, height: 2 mm, resolution: 2.12 μm/pixel)



3.4 Microstructure and Grain Structure Analysis

Figure 9 shows the optical and scanning electron micrographs for the different processing conditions (S1: Fig. 9a–d, S3: Fig. 9e–h, S9: Fig. 9i–l, and S12: Fig. 9m–p). The typical layer-wise structure with melt pool boundaries and solidification cracks along the build direction can be seen from the optical micro-graphs for cases S1 (Fig. 9a), S3 (Fig. 9e), and S9 (Fig. 9i). As observed before, the base plate heating

increases the size of the melt pool (S9, Fig. 9i) due to the additional heat input. The scanning strategy was turned 90° after each layer, as seen in the SEM picture. As a result, even layers have a cross-section of a single scan track (parallel to the laser scan), whereas odd layers have various half-cylindrical melt pools (cross-sections normal to the laser scan). Additionally, the overlap between the adjacent and the following layers can be seen. In these micro-graphs, cracks are also visible for cases S1, S3, and S9. The microstructure

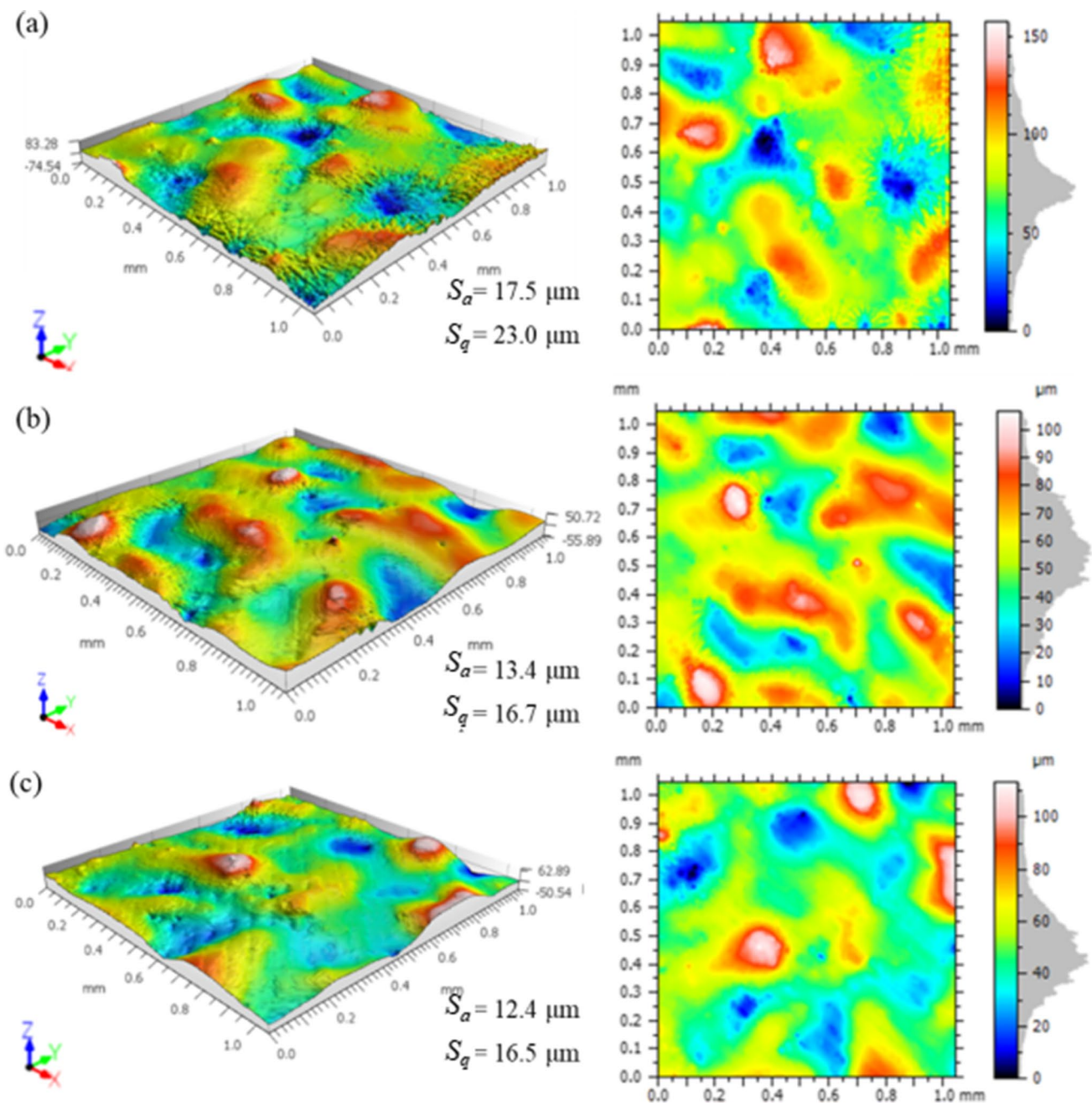


Fig. 8 Surface topography results obtained from 3D Optical Profilometry for different samples **a** *S1*, **b** *S2*, and **c** *S3*

Table 4 Contact-type mechanical profilometry results for *S1*, *S2*, and *S3*

Sample	R_a (μm)	R_q (μm)
<i>S1</i>	21.03 ± 0.63	25.34 ± 0.74
<i>S2</i>	14.61 ± 0.12	17.62 ± 0.31
<i>S3</i>	9.91 ± 0.21	12.51 ± 0.42

generated by LPBF results in a very fine cellular-dendritic grain microstructure because of the high cooling rates. When examining the microstructure with LPBF at greater magnifications (Fig. 9b–d), a very fine microstructure can be seen. As shown in Fig. 9e–f, remelting scan partially melts the columnar dendritic grains of the first tracks. Thus, the orientation of the new grains is changed, which eventually leads to a change in the crack orientations. This phenomenon reduces the crack length and thus produces multiple small-sized cracks. A similar trend is also followed

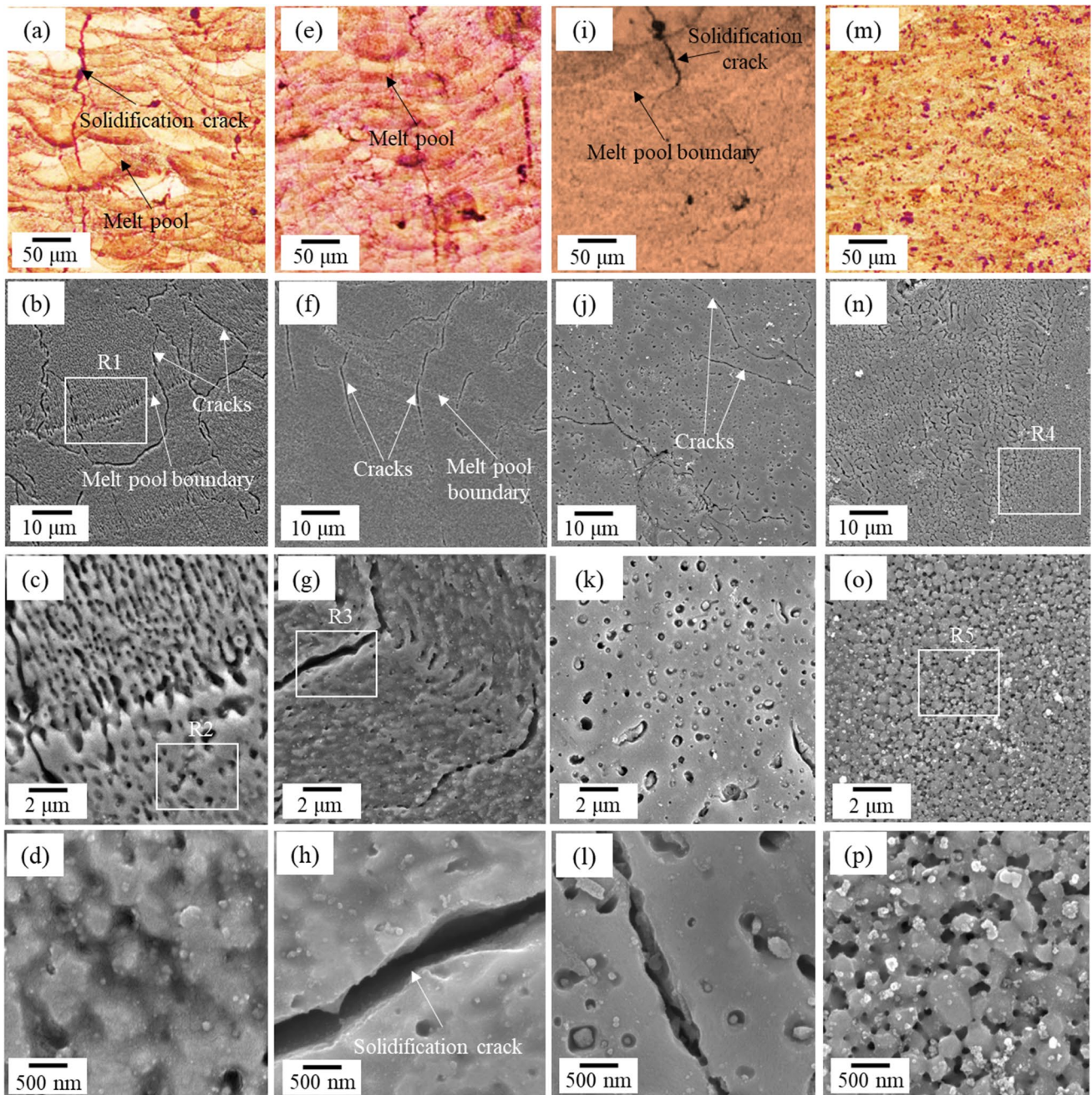


Fig. 9 Optical microscopy and FESEM micrographs of LPBF fabricated samples **a–d** S1, **e–h** S3, **i–l** S9, and **m–p** S12

in the remelted base plate heating case (Fig. 9 i–j). Here, the cracks are reduced in number due to large grains but increase lengthwise. The reduction in temperature gradient because of the base plate heating helps remove the crack generation phenomena. However, some cracks are presented, shown in the FESEM image (Fig. 9j). When looking closer at the melt pool's boundary (i.e., R2 in Fig. 9c–d), certain small pores may be seen that are more frequent than those seen inside the melt pool. Solidification shrinkage is the reason for that. However, most of them have a very spherical

form, which indicates that vapor phases like Zn or Mg generate them. Two separate apparent phases, dark and light phases, can be seen in Fig. 9k micro-graphs. As shown in Fig. 9m–p, because of the relatively uniform distribution and the concentration of nano TiC, enough TiC incorporated into Al7075 alloys is expected to be rather substantial, potentially improving the growth limitation impact of nanoparticles. Some nano TiC reinforcement and other alloying elements are pushed toward solidification due to continual solidification. Nano TiC reinforcement is very effective at pushing

the grain boundary to physically restrain grain growth and provide a significant growth limitation factor. These results significantly improve the microstructure of nano-reinforced Al7075, as illustrated in Fig. 9n–p, where aluminium dendrites are refined to fine equiaxed grains. As a result of the outstanding refinement of its microstructure, the mechanical characteristics of nano-reinforced Al7075 with dense microstructure are proportionally enhanced.

In Fig. 10, the first row shows the EBSD inverse pole figures, and the second row shows the angular grain boundary combination at different angle ranges for samples *S1*, *S3*, *S9*, and *S12*. The third row shows the combined graphs of number fraction vs. disorientation angle and area fraction vs. grain size variations for different cases. The grain size of the Al7075 was assessed using an EBSD color map, and the grain size variation as a function of remelting, base plate heating, and 4 wt% TiC nano reinforcement is shown in Fig. 10 and computed average grain sizes of $59.30 \pm 28.37 \mu\text{m}$, $57.8 \pm 28.15 \mu\text{m}$, $118.95 \pm 66.63 \mu\text{m}$, and $1.88 \pm 0.58 \mu\text{m}$ in Fig. 10i–l respectively. In the LPBF

fabricated Al7075 alloys, remelting techniques had little effect on the microstructure. Base plate heating increases the grain size due to low thermal gradient, but reinforcement with 4 wt% nano TiC considerably refined the Al7075 grains. The *S1*, *S3*, and *S9* samples are characterized by massive columnar grains that formed epitaxially along the build direction (B.D. [001]) shown by the IPF color, terminating at lengths of hundreds of micron meters, as shown in Fig. 10e–g. In addition, crystallographic features in terms of grain boundary orientation angles, such as low-angle grain boundaries (LAGBs, 0–15°) and high-angle grain boundaries (HAGBs, > 15°), can be utilized to investigate material behavior. The red, green, and blue color grain boundaries in Fig. 10e–h shows an angle of 0–5°, 5–15°, and greater than 15°. From Fig. 10i–l, it was clear that the *S1* had only 6.1% HAGBs, whereas *S3* produces 41.9% HAGBs due to the fragmentation of solidified grains and differences in first and remelted scan grain orientations. Base plate heating sample *S9* produces 0.8% HAGBs only due to grain size increase due to a lower temperature gradient. The *S12* had more

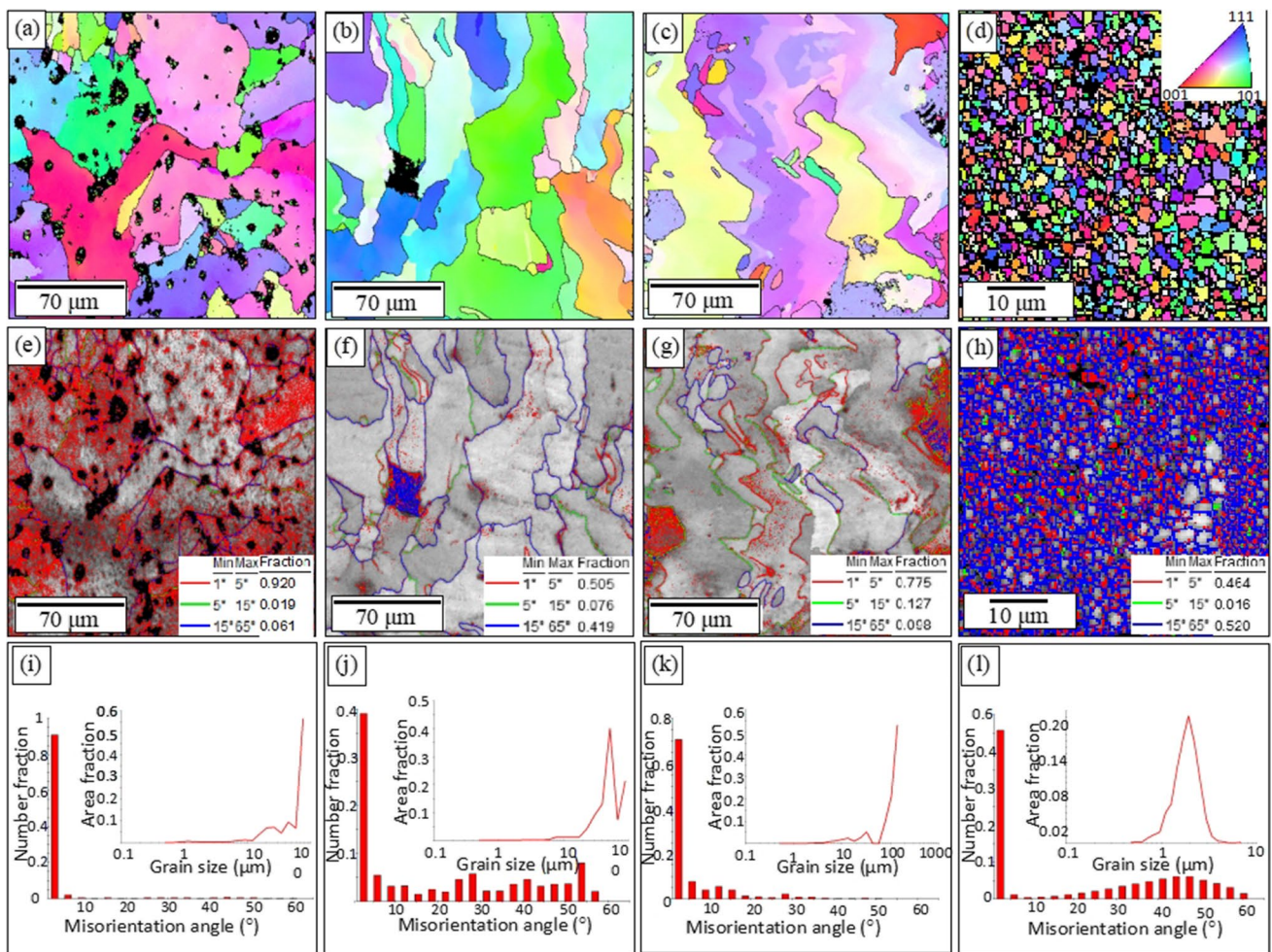


Fig. 10 EBSD map, grain boundaries, and grain size and misorientation map. *S1* (a, e, i), *S3* (b, f, j), *S9* (c, g, k), *S12* (d, h, l)

HAGBs (52%). The insertion of TiC nano-reinforcement into an Al7075 matrix reduces the development of grains. One of the most significant advantages of the grain refining process for enhancing mechanical properties is the presence of a strain field with more dislocations.

3.5 Cracking Formation Mechanisms in Al7075 Alloy

According to the findings shown in Fig. 9, Cracking began and spread parallel to the build direction along the columnar grain boundaries in the Al7075 alloy. This indicates that during LPBF processing, the intergranular zones were vulnerable to cracking. Cracking is formed by two main mechanisms: 1) solidification cracking and 2) liquation cracking, according to earlier research on the standard welding processes [21]. The solidification cracking happens in the fusion zone of a melt pool as a result of thermal stresses as shown in Fig. 1d. While the liquation cracking frequently develops outside the MP in the heat-affected zone as a result of low melting point phases, inclusions, and microstructure along grain boundaries (such as eutectic components) melting, which is easily create a route for the cracking as shown in Fig. 1c.

In single layer track study of Remelted S2 case (v1st melt: 200 mm/s, v2nd melt: 800 mm/s) as shown in Fig. 11, the crack is initiated and propagated within the melt pool in the build direction, thus demonstrating the Solidification cracking phenomenon in the single melting study.

According to optical microscopy and FESEM findings shown in Fig. 9, the majority of the cracks originated within the melt pools and crossed multiple layers, which is a characteristic of hot-tearing cracks (Solidification cracks) [43]. Additionally, because liquation cracking is linked to

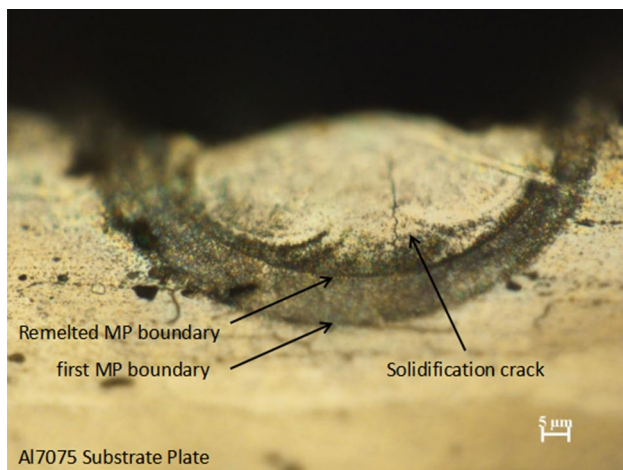


Fig. 11 Solidification crack in optical microscopy of a single layer of S2 parameter on Al7075 substrate plate

microstructural melting, the higher the energy input, the more likely it is that liquation cracking will take place [44]. However, in the current SLM-fabricated alloys, the crack fraction has decreased with an increase in base plate heating (Fig. 9 i) which led to high energy input in the process, thus, liquation is not the dominant mechanism of cracking.

3.6 Phase Analysis and Mechanical Testing Results

The phase analysis of the different samples was done using X-ray diffraction (XRD). Figure 12a shows the XRD results for 2θ angles ranging from 30° to 100° . The (111) at 38.45° , (200) at 44.70° , (220) at 66.08° , (211) at 78.18° , and (222) at 82.41° are the major crystallographic orientations for Al and (111) at 36.40° , (200) at 41.68° , (220) at 61.18° and (311) at 72.86° are the orientations for the FCC TiC. On the other hand, several less strong peaks are detected, which represent $MgZn_2$ (circle) and Al_2CuMg (triangle). Different intensities are found for the crystallographic orientations of Al in the LPBF sample. For pure Al7075, the crystallographic orientation (200) is dominant, and (220) has a greater intensity than the other alloys. As per the comparison of all peaks, it is concluded that no intermetallic phase was created in the LPBF of TiC-reinforced Samples. The XRD graphs for the samples are nearly identical, implying that the remelting and base plate heating had no deleterious influence on the crystalline nature.

Micro-hardness measurements were taken for the determination of mechanical characteristics of the Al7075 generated via LPBF, shown in Fig. 12b. Table 5 shows the hardness of Al7075 following various processing parameters. The hardness drop is visible, mostly due to grain coarsening and the relief of residual stresses in the LPBF printed samples as an increase in base plate heating temperature. The slight increase in hardness is also shown in remelted samples. That is because of the grain refinement due to the remelting of columnar grains. The hardness of cold-rolled and homogenized Al7075 is 135 HV, nearly the same as that of 122.49 ± 7.43 for S1. However, the traditionally manufactured heat-treated Al7075 -T6 has a much greater hardness value of 175 HV. The hardness value is increased for the S10 sample to 157.62 ± 5.61 HV because of the significant grain refinements due to the addition of nano-reinforcements. In the S12 sample case, hardness is increased further to 181.72 ± 23.52 HV.

Figure 12c shows the tensile test results, which were carried out on LPBF printed samples (S1, S2, and S12). According to grain boundary strengthening, the tensile strength of Al7075 is affected by grain size. The S12 sample has a fine structure, thus having a high tensile strength. The ultimate tensile strength and elongation for the S1, S2, and S12 are 58.26 MPa, 115.47 MPa, 214.75 MPa, 1.83%, 2.93%, and 8.12%, respectively. In the case of S12, a higher level of tensile strength is achieved due

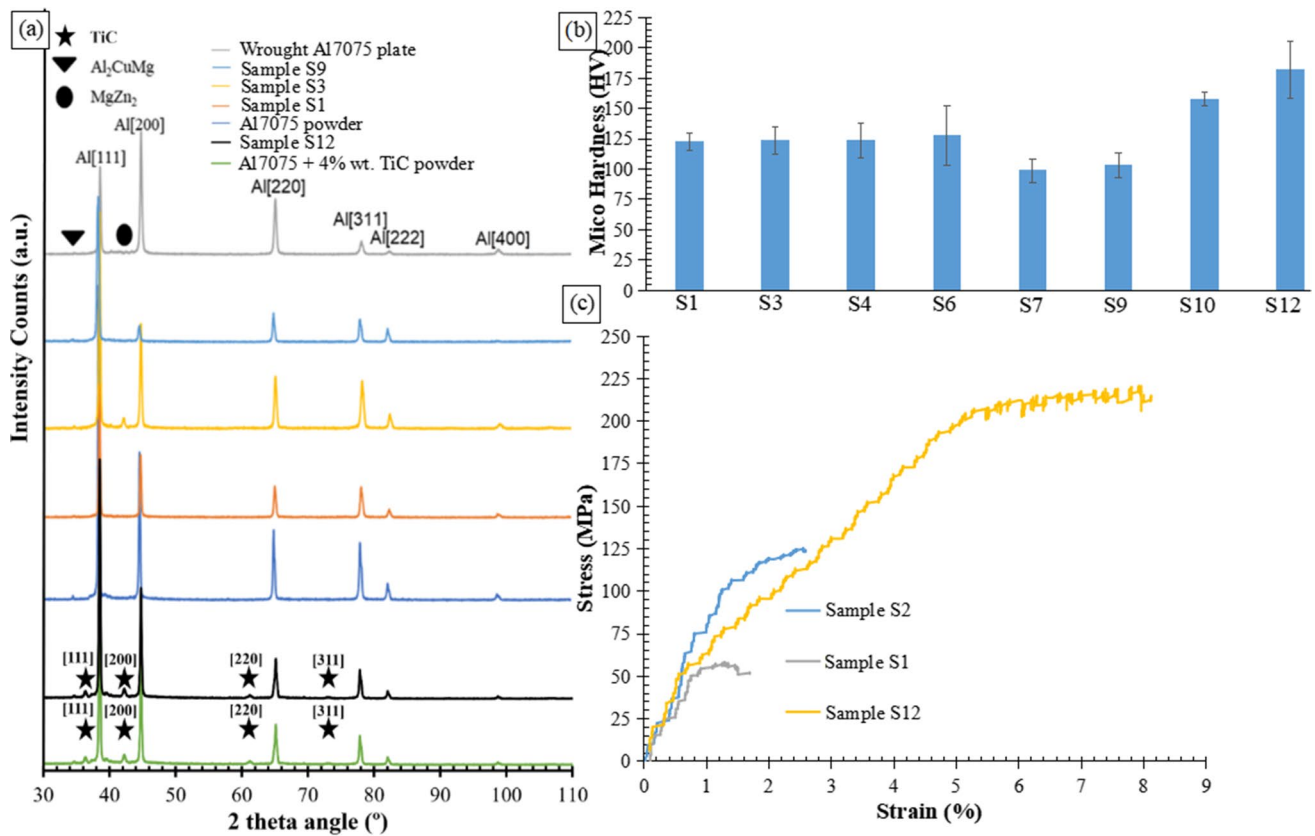


Fig. 12 a XRD plot, b Microhardness results, and c Tensile testing results for various processing conditions (Table 3)

Table 5 The comparison of the hardness test results of different samples

Sample	S1	S3	S4	S6	S7	S9	S10	S12
HV	122.49 ± 7.43	123.57 ± 11.5	120.72 ± 13.09	121.44 ± 22.75	98.97 ± 9.71	103.28 ± 10.02	157.62 ± 5.61	181.72 ± 23.52

to fine equiaxed grains. Even though, we eliminated cracks and reduced porosity in optimized sample *S12* (first scan speed = 200 mm/s, remelting speed = 1600 mm/s, and 4 wt% TiC nano reinforcement). The presence of porosity in the *S12* (optimized condition) sample can be seen in the 3D reconstructed X-ray tomography result (Fig. 7b). The presence of pores causes the initiation of failure of the fabricated sample, resulting in a decrease in mechanical strength. Hot Isostatic Pressing and heat treatment helps to improve the mechanical qualities of parts made by additive manufacturing, it was not used in this work to maintain the similarity between MMCs and Al7075 samples made in different processing conditions.

4 Conclusions

In this work, ramped-down high-speed remelting, high-temperature base plate heating, and the TiC nano-reinforcement addition have been utilized to control the cracking behavior, porosity formation, and build surface quality. The following conclusions are drawn from this study:

- The LPBF process parameter optimization (88.24% density), application of ramped-down high-speed remelting (95.13% density), and base plate heating condition (96.03% density) are not sufficient to obtain

crack-free samples. However, adding 4 wt% TiC nano reinforcement in the Al7075 matrix fabricates crack-free samples (99.71% density).

- The ramped-down remelting approach significantly reduces the lack of fusion porosity, eliminates unmelted powder particles, and eventually improves the fabricated part surface finish. The top surface roughness measurement suggests that the S2 ($P=95$ W, $v_{1st}=200$ mm/s, $v_{2nd}=800$ mm/s) improves by 30.5% surface quality, S3 ($P=95$ W, $v_{1st}=200$ mm/s, $v_{2nd}=1600$ mm/s) improves to 52.88% average surface quality compared to the S1 ($P=95$ W, $v_{1st}=200$ mm/s) sample surface quality.
- In the LPBF of Al7075 alloy, the cracks originated within the melt pools and crossed multiple layers, which suggests the solidification cracking dominance over liquation cracking.
- The single melting based LPBF samples have large columnar dendritic grains with cracks in the build direction. The usage of substrate plate heating produced bigger grains with a smaller number of cracks. The ramped-down remelting remelts the solidified layer columnar grains and generated new grains in different orientations, resulting in grain fragmentation and reduced crack length. The 4 wt% TiC nano reinforcement and remelting achieved defect-free fine equiaxed grain structure (average grain size: 1.88 μm).
- TiC nano reinforcements act as effective heterogeneous nucleation sites and produce small equiaxed grain microstructure, resulting in the improvement of mechanical properties of Al7075 (Tensile strength of 214.75 MPa, elongation of 8.12%, and hardness of 181.72 ± 23.52 HV), in addition to the growth restriction factor by pinning behavior on grain boundaries.

Declarations

Conflict of interests The authors did not receive support from any organization for the submitted work. All authors certify that they have no affiliation with or involvement in any organization or entity with any financial interest or non-financial interest in the subject matter or materials discussed in this manuscript.

References

1. I. Campbell, D. Bourell, I. Gibson, Additive manufacturing: rapid prototyping comes of age. *Rapid Prototyp. J.* **18**, 255–258 (2012)
2. T. DebRoy, H.L. Wei, J.S. Zuback, T. Mukherjee, J.W. Elmer, J.O. Milewski, A.M. Beese, A.D. Wilson-Heid, A. De, W. Zhang, Additive manufacturing of metallic components—process, structure and properties. *Prog. Mater. Sci.* **92**, 112–224 (2018)
3. S.A. Khairallah, A.A. Martin, J.R. Lee, G. Guss, N.P. Calta, J.A. Hammons, M.H. Nielsen, K. Chaput, E. Schwalbach, M.N. Shah, M.G. Chapman, Controlling interdependent meso-nanosecond dynamics and defect generation in metal 3D printing. *Science* **368**(6491), 660–665 (2020)
4. Q. Guo, C. Zhao, M. Qu, L. Xiong, L.I. Escano, S.M.H. Hojjatzadeh, N.D. Parab, K. Fezzaa, W. Everhart, T. Sun, L. Chen, In-situ characterization and quantification of melt pool variation under constant input energy density in laser powder bed fusion additive manufacturing process. *Addit. Manuf.* **28**, 600–609 (2019)
5. N.T. Aboulkhair, M. Simonelli, L. Parry, I. Ashcroft, C. Tuck, R. Hague, 3D printing of aluminium alloys: additive manufacturing of aluminium alloys using selective laser melting. *Prog. Mater. Sci.* **106**, 100578 (2019)
6. Y. Cao, H.L. Wei, T. Yang, T.T. Liu, W.H. Liao, Printability assessment with porosity and solidification cracking susceptibilities for a high strength aluminum alloy during laser powder bed fusion. *Addit. Manuf.* **46**, 102103 (2021)
7. C. Galy, E. Le Guen, E. Lacoste, C. Arvieu, Main defects observed in aluminum alloy parts produced by SLM: from causes to consequences. *Addit. Manuf.* **22**, 165–175 (2018)
8. E. Louvis, P. Fox, C.J. Sutcliffe, Selective laser melting of aluminium components. *J. Mater. Process. Technol.* **211**(2), 275–284 (2011)
9. D.G. Eskin, *Physical Metallurgy of Direct Chill Casting of Aluminum Alloys* (CRC Press, Boca Raton, 2008)
10. V.N. Moiseyev, *Titanium alloys: Russian Aircraft and Aerospace Applications* (CRC Press, Boca Raton, 2005)
11. S. Kou, A criterion for cracking during solidification. *Acta Mater.* **88**, 366–374 (2015)
12. T. Soysal, S. Kou, A simple test for assessing solidification cracking susceptibility and checking validity of susceptibility prediction. *Acta Mater.* **15**(143), 181–197 (2018)
13. Q. Guo, M. Qu, L.I. Escano, S.M.H. Hojjatzadeh, Z. Young, K. Fezzaa, L. Chen, Revealing melt flow instabilities in laser powder bed fusion additive manufacturing of aluminum alloy via in-situ high-speed X-ray imaging. *Int. J. Mach. Tools Manuf.* **175**, 103861 (2022)
14. J. Zhang, B. Song, Q. Wei, D. Bourell, Y. Shi, A review of selective laser melting of aluminum alloys: processing, microstructure, property and developing trends. *J. Mater. Sci. Technol.* **35**(2), 270–284 (2019)
15. M. Opprecht, J.P. Garandet, G. Roux, C. Flament, M. Soulier, A solution to the hot cracking problem for aluminium alloys manufactured by laser beam melting. *Acta Mater.* **197**, 40–53 (2020)
16. X. Chang, G. Chen, W. Sun, H. Zhang, G. Chu, X. Zhang, F. Han, W. Zhang, Z. Du, Microstructures, mechanical properties and solidification mechanism of a hot tearing sensitive aluminum alloy asymmetric part fabricated by squeeze casting. *J. Alloy. Compd.* **886**, 161254 (2021)
17. A.M. Khalil, I.S. Loginova, A.N. Solonin, A.O. Mosleh, Controlling liquation behavior and solidification cracks by continuous laser melting process of AA-7075 aluminum alloy. *Mater. Lett.* **277**, 128364 (2020)
18. K.H. Grote, E.K. Antonsson (eds.), *Springer Handbook of Mechanical Engineering* (Springer, Berlin, 2009), pp.721–723
19. B. Kuźnicka, R. Dziedzic, P. Szymczyk, E. Chlebus, Consequences of rapid heating of Al–Cu alloy and martensitic stainless steel. *Eng. Fail. Anal.* **26**, 192–202 (2012)
20. F.M. Ghaini, M. Sheikhi, M.J. Torkamany, J. Sabbaghzadeh, The relation between liquation and solidification cracks in pulsed laser welding of 2024 aluminium alloy. *Mater. Sci. Eng. A* **519**(1–2), 167–171 (2009)

21. S. Kou, Predicting susceptibility to solidification cracking and liquation cracking by CALPHAD. *Metals* **11**(9), 1442 (2021)
22. W. Reschetnik, J.P. Brüggemann, M.E. Aydinöz, O. Grydin, K.P. Hoyer, G. Kullmer, H.A. Richard, Fatigue crack growth behavior and mechanical properties of additively processed EN AW-7075 aluminium alloy. *Proced. Struct. Integr.* **2**, 3040–3048 (2016)
23. W. Stopyra, K. Gruber, I. Smolina, T. Kurzynowski, B. Kuźnicka, Laser powder bed fusion of AA7075 alloy: influence of process parameters on porosity and hot cracking. *Addit. Manuf.* **35**, 101270 (2020)
24. N. Kaufmann, M. Imran, T.M. Wischeropp, C. Emmelmann, S. Siddique, F. Walther, Influence of process parameters on the quality of aluminium alloy EN AW 7075 using selective laser melting (SLM). *Phys. Proced.* **83**, 918–926 (2016)
25. R. Mertens, S. Dadbakhsh, J. Van Humbeeck, J.P. Kruth, Application of base plate preheating during selective laser melting. *Proced. Cirp* **74**, 5–11 (2018)
26. E.G. Brodie, A.E. Medvedev, J.E. Frith, M.S. Dargusch, H.L. Fraser, A. Molotnikov, Remelt processing and microstructure of selective laser melted Ti25Ta. *J. Alloy. Compd.* **820**, 153082 (2020)
27. D. Zhang, J. Yu, H. Li, X. Zhou, C. Song, C. Zhang, S. Shen, L. Liu, C. Dai, Investigation of laser polishing of four selective laser melting alloy samples. *Appl. Sci.* **10**(3), 760 (2020)
28. J. Ghorbani, J. Li, A.K. Srivastava, Application of optimized laser surface re-melting process on selective laser melted 316L stainless steel inclined parts. *J. Manuf. Process.* **56**, 726–734 (2020)
29. B. Shen, H. Li, S. Liu, J. Zou, S. Shen, Y. Wang, T. Zhang, D. Zhang, Y. Chen, H. Qi, Influence of laser post-processing on pore evolution of Ti–6Al–4V alloy by laser powder bed fusion. *J. Alloy. Compd.* **818**, 152845 (2020)
30. Z. Yu, Y. Zheng, J. Chen, C. Wu, J. Xu, H. Lu, C. Yu, Effect of laser remelting processing on microstructure and mechanical properties of 17–4 PH stainless steel during laser direct metal deposition. *J. Mater. Process. Technol.* **284**, 116738 (2020)
31. R. Koike, T. Misawa, T. Aoyama, M. Kondo, Controlling metal structure with remelting process in direct energy deposition of Inconel 625. *CIRP Ann.* **67**(1), 237–240 (2018)
32. J. Zhou, X. Han, H. Li, S. Liu, J. Yi, Investigation of layer-by-layer laser remelting to improve surface quality, microstructure, and mechanical properties of laser powder bed fused AlSi10Mg alloy. *Mater. Des.* **210**, 110092 (2021)
33. P.C. Collins, D.A. Brice, P. Samimi, I. Ghamarian, H.L. Fraser, Microstructural control of additively manufactured metallic materials. *Annu. Rev. Mater. Res.* **46**(1), 63–91 (2016)
34. W. Kurz, C. Bezençon, M. Gäumann, Columnar to equiaxed transition in solidification processing. *Sci. Technol. Adv. Mater.* **2**(1), 185 (2001)
35. D. Ruvalcaba, R.H. Mathiesen, D.G. Eskin, L. Arnberg, L. Katgerman, In situ observations of dendritic fragmentation due to local solute-enrichment during directional solidification of an aluminum alloy. *Acta Mater.* **55**(13), 4287–4292 (2007)
36. C.J. Todaro, M.A. Easton, D. Qiu, D. Zhang, M.J. Bermingham, E.W. Lui, M. Brandt, D.H. StJohn, M. Qian, Grain structure control during metal 3D printing by high-intensity ultrasound. *Nat. Commun.* **11**(1), 142 (2020)
37. J.H. Martin, B.D. Yahata, J.M. Hundley, J.A. Mayer, T.A. Schae-dler, T.M. Pollock, 3D printing of high-strength aluminium alloys. *Nature* **549**(7672), 365–369 (2017)
38. J. Bi, Z. Lei, Y. Chen, X. Chen, Z. Tian, J. Liang, X. Zhang, X. Qin, Microstructure and mechanical properties of a novel Sc and Zr modified 7075 aluminum alloy prepared by selective laser melting. *Mater. Sci. Eng. A* **768**, 138478 (2019)
39. M.L. Montero-Sistiaga, R. Mertens, B. Vrancken, X. Wang, B. Van Hooreweder, J.P. Kruth, J. Van Humbeeck, Changing the alloy composition of Al7075 for better processability by selective laser melting. *J. Mater. Process. Technol.* **238**, 437–445 (2016)
40. W. Wu, C. Gao, Z. Liu, K. Wong, Z. Xiao, Laser powder bed fusion of crack-free TiN/Al7075 composites with enhanced mechanical properties. *Mater. Lett.* **282**, 128625 (2021)
41. Q. Tan, Z. Fan, X. Tang, Y. Yin, G. Li, D. Huang, J. Zhang, Y. Liu, F. Wang, T. Wu, X. Yang, A novel strategy to additively manufacture 7075 aluminium alloy with selective laser melting. *Mater. Sci. Eng. A* **821**, 141638 (2021)
42. W. Li, Y. Yang, J. Liu, Y. Zhou, M. Li, S. Wen, Q. Wei, C. Yan, Y. Shi, Enhanced nanohardness and new insights into texture evolution and phase transformation of TiAl/TiB₂ in-situ metal matrix composites prepared via selective laser melting. *Acta Mater.* **136**, 90–104 (2017)
43. J.C. Lippold, S.D. Kiser, J.N. DuPont, *Welding Metallurgy and Weldability of Nickel-Base Alloys* (John Wiley & Sons, Hoboken, 2009)
44. S. Kou, *Welding Metallurgy*, 2nd edn. (John Wiley & Sons, Hoboken, 2003), pp. 223–225

Publisher's Note Springer Nature remains neutral with regard to jurisdictional claims in published maps and institutional affiliations.

Springer Nature or its licensor (e.g. a society or other partner) holds exclusive rights to this article under a publishing agreement with the author(s) or other rightsholder(s); author self-archiving of the accepted manuscript version of this article is solely governed by the terms of such publishing agreement and applicable law.